

## Supplemental Material

### Chemically Resolved Interface Structure of Epitaxial Graphene on SiC(0001)

Jonathan D. Emery<sup>1</sup>, Blanka Detlefs<sup>2</sup>, Hunter J. Karmel<sup>1</sup>, Luke O. Nyakiti<sup>3</sup>, D. Kurt Gaskill<sup>3</sup>, Mark C. Hersam<sup>1,4</sup>, Jörg Zegenhagen<sup>2</sup>, Michael J. Bedzyk<sup>1,5</sup>

1. Department of Materials Science and Engineering, Northwestern University, Evanston, Illinois 60208, USA

2. European Synchrotron Radiation Facility, BP 220, 38043, Grenoble, Cedex 9, France.

3. US Naval Research Lab, Washington, District of Columbia 20375, USA

4. Department of Chemistry, Northwestern University, Evanston Illinois, 60208, USA

5. Department of Physics and Astronomy, Northwestern University, Evanston Illinois, 60208, USA

### X-ray Standing Wave

In the dipole approximation for the photoelectric effect, the normalized  $E_\gamma$ -dependent photoelectron yield is:

$$Y_j(E_\gamma) = 1 + R(E_\gamma) + 2p\sqrt{R(E_\gamma)} f_j \cos[\phi(E_\gamma) - 2\pi P_j], \quad (\text{S1})$$

where  $R$  is the Bragg reflectivity,  $E_\gamma$  is the incident photon energy,  $p$  is the polarization factor, and  $\phi$  is the XSW phase. By fitting Eq. S1 to the photoelectron yield data from an atomic species with a specific chemical state,  $j$ , one can extract the Fourier amplitude and phase  $f_j$  and  $P_j$  to resolve the chemically sensitive atomic density profile,  $N_j(z)$ , which is defined in the main text (Eq. 1).

### Experimental:

The 0.5 and 1.3 ML samples were grown from nominally on-axis nitrogen-doped 6H-SiC(0001) substrates graphitized by direct current flashing in UHV. The 0.5 ML sample was processed with a 550° C overnight degas followed by sequential flashes of 1000° C for 5 minutes, 1100° C for 5 minutes and 1200° C for 1 minute. The 1.3 ML sample was processed using the same degas and

1000° C and 1100° C anneals, but were treated with additional anneals at 1200° C, 1250° C, and 1300° C for 2, 2, and 1 minute, respectively.

EG synthesis of the 1.7 ML sample was carried out in a commercial hot-wall Aixtron/Epigress VP508 chemical vapor deposition reactor. Prior to graphene growth, substrates underwent an *in situ* H<sub>2</sub> etch at 1520°C for 30 minutes. After etching, H<sub>2</sub> was purged, and the subsequent EG formation process was conducted under a flowing Ar ambient of 10 standard liters per minute at 100 mbar at 1540° C for 30 minutes.

XSW-XPS measurements were performed in UHV ( $1 \times 10^{-10}$  Torr) at the ID32 beam line[1] of the European Synchrotron Radiation Facility. The incident photon energy,  $E_\gamma$ , was set near the SiC(0006) back-reflection condition (Bragg angle,  $\theta_B \sim 88^\circ$  and  $E_\gamma \sim 2.450$  keV) using a Si(111) double crystal monochromator. The photon flux at the sample surface was  $10^{12}$  photons/s within a  $0.1 \times 0.4$  mm<sup>2</sup> spot size. Photoelectrons were collected with a SPECS-PHOIBOS 225 electron analyzer positioned with analyzer axis mounted parallel to the X-ray polarization

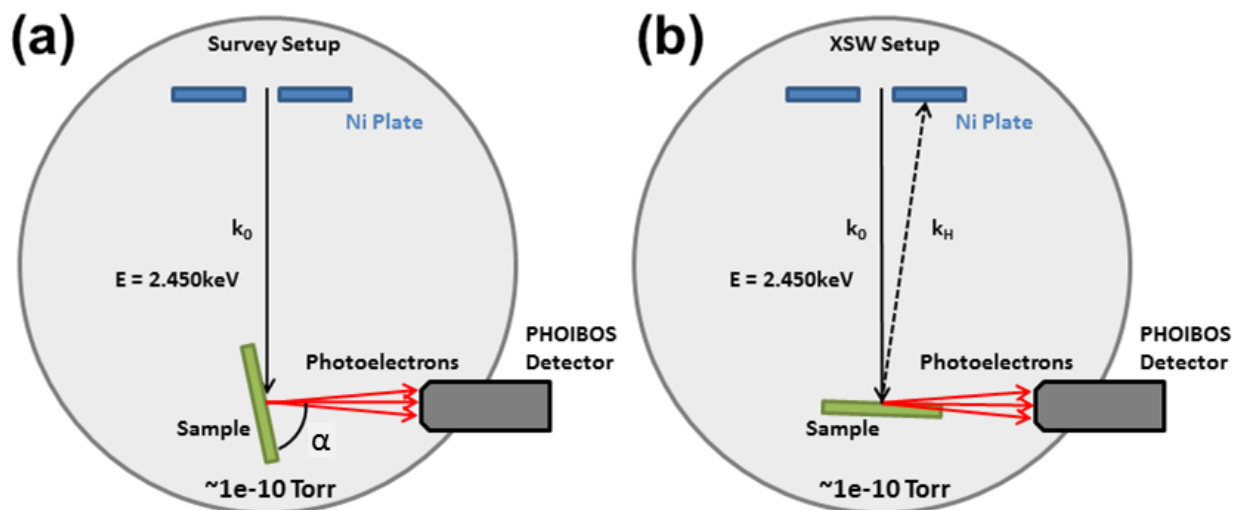


**FIG. S1:** Experimental geometries for both (a) conventional XPS ( $\alpha \sim 78^\circ$ ) used for survey scans and (b) highly surface-sensitive grazing-emission XPS ( $\alpha \sim 2^\circ$ ) used for XSW measurements. Tuning the emission angle to  $\alpha \sim 2^\circ$  improves surface sensitivity by effectively decreasing the sampling depth of the photoelectrons originating from deep within the crystal as compared to those nearer to the surface. The effective sampling depth is  $\Lambda_e \sim \text{IMFP} \sin(\alpha)$

## LEED:

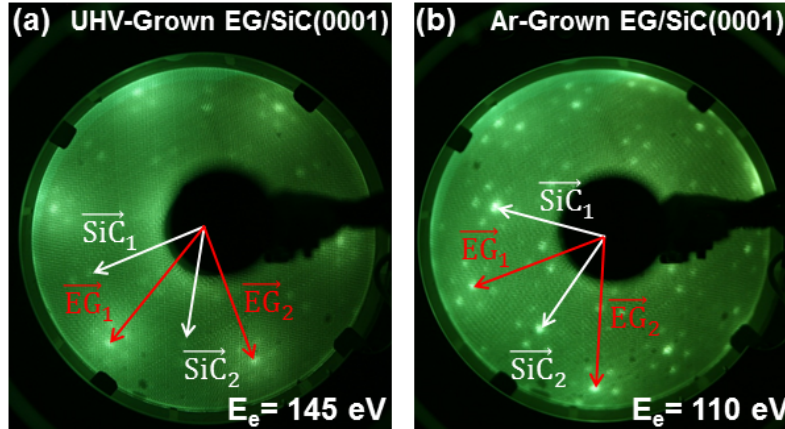


**FIG. S2:** LEED patterns for both 1.3 ML UHV-grown (a) and 1.7 ML Ar-grown (b) EG/SiC(0001). Each image shows the typical pattern with bright  $1 \times 1$  EG (red arrow) and  $1 \times 1$  SiC (white arrow) spots. The spots arranged in a hexagon about the EG spots are due to the  $6\sqrt{3} \times 6\sqrt{3}$   $R30^\circ$  reconstructed interfacial layer. Ar-growth resulted in larger surface domains, subsequently resulting in the sharper LEED pattern in (b).

## XPS Survey:

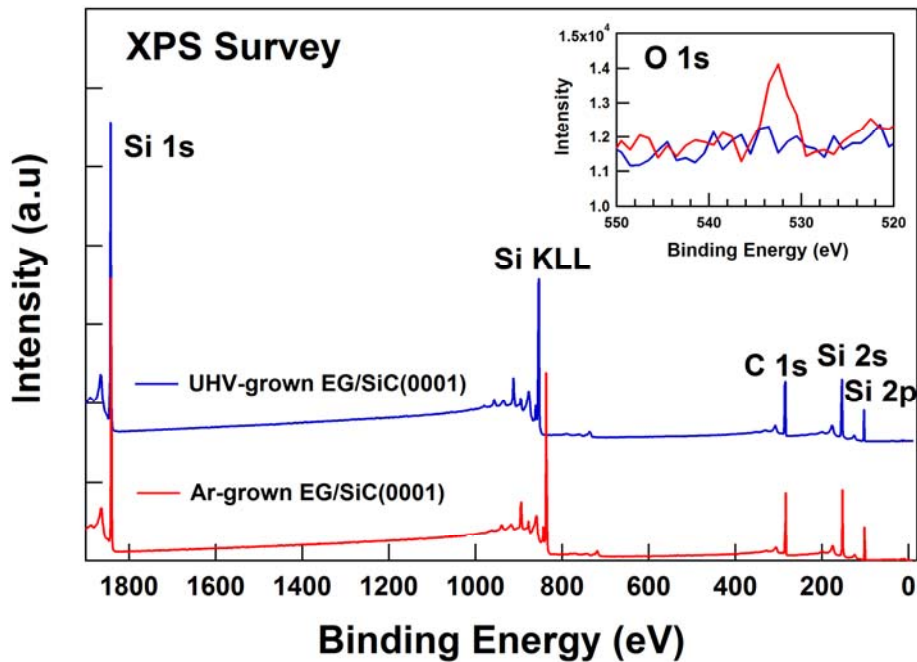


**Figure S3:** Survey spectra for 1.3 ML UHV-grown EG/SiC(0001) (blue) and 1.7 ML Ar-grown EG/SiC(0001) (red). Spectra were acquired with a photoemission angle  $\alpha \sim 78^\circ$  (Fig. S1(a)) and using incident beam energies of 2.450 and 2.465 keV, respectively. The inset shows a weak O 1s signal present in the Ar-grown spectrum associated with a small amount of silicon oxide near-surface contamination. Oxide surface contamination is estimated in the text.

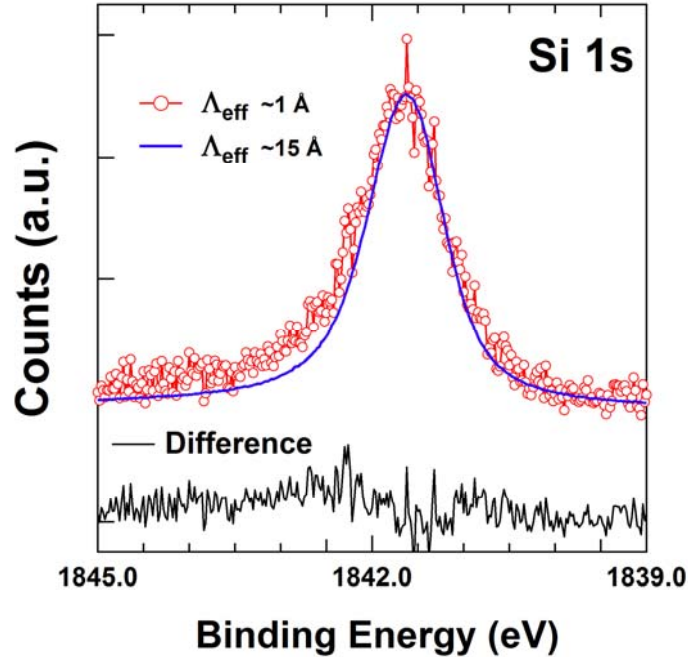


**FIG. S4:** Overlay of Si 1s spectra from 1.3 ML UHV-grown EG/SiC(0001) taken at emission angles  $\alpha \sim 78^\circ$  (blue) and  $\alpha \sim 2^\circ$  (red). The peak width broadens by  $\sim 20\%$  when measured using the  $\alpha = 2^\circ$  geometry, indicating increased spectral contribution from strained surface Si species. The difference trace is shown in black.

direction in order to minimize the influence of non-dipole contributions to the photoelectron yield [2, 3]. The FWHM total energy resolution of the photoelectron spectra was  $\sim 0.60$  eV, which accounts for the FWHM incident beam bandwidth of 0.34 eV.

X-ray reflectivity measurements were performed in ambient at the Advanced Photon Source, Dupont-Northwestern-Dow Collaborative Access Team 5ID-C station using  $E_\gamma = 17.0$  keV X-rays collimated to a  $0.1 \times 2.0$  mm<sup>2</sup> spot size with a flux of  $\sim 5 \times 10^{11}$  photons/s. The reflected intensity at the specular condition was measured using an area detector [4, 5]. Below  $q_z \sim 0.5 \text{ \AA}^{-1}$ , the finite surface domain size of UHV-grown samples resulted in significant transverse broadening of the specular rod, which inhibited accurate integration of the XRR signal.

### Peak Fitting:

For all samples, the  $C_{\text{Bulk}}$ ,  $S_1$  and  $S_2$  peaks are fit using either pseudo-Voigt functions or with a summation of Gaussian and Lorentzian lineshapes (SGL):

$$SGL(x; \gamma, x_0, \eta) = (1 - \eta) \text{Exp}[-4 \ln 2 \left(\frac{x - x_0}{F}\right)^2] + \eta \left(\frac{1}{1 + 4 \left(\frac{x - x_0}{F}\right)^2}\right) \quad \text{Eq. S1}$$

where the components are weighted by factor  $\eta$  and have common positions  $x_0$ , and widths  $F$ . To account for the slight asymmetry in the Si 1s peak, we used a modified  $a$ -SGL function [6]. To account for the metallic nature of the EG, the peak is fit with a Gaussian-broadened Doniach-Sunjc [7] profile (DS):

**Table S1:** Fitting parameters for C 1s and Si 1s spectra from EG/SiC(0001) samples. SGL denotes a summation Gaussian-Lorentzian,  $a$ -SGL denotes an asymmetric SGL, with asymmetry factors  $a$  and  $b$ . DS represents a Doniach-Sunjc curve with asymmetry factor  $\epsilon$ .

<b>0.5 ML UHV-grown EG/SiC(0001)</b>						
	<b>Si 1s</b>		<b>C 1s</b>			
<b>Component</b>	<b>Bulk Si</b>	<b>SiO<sub>x</sub></b>	<b>Bulk C</b>	<b>EG</b>	<b>S<sub>1</sub></b>	<b>S<sub>2</sub></b>
<b>Lineshape</b>	$a$ -SGL	SGL	SGL	DS	SGL	SGL
<b><math>\epsilon</math> or <math>a/b</math></b>	0.25,0.09	-	-	0.105	-	-
<b><math>\eta</math></b>	0.55	0.25	0.20	-	0.10	0.20
<b>E<sub>B</sub></b>	1841.70	1844.40	283.80	284.80	285.15	285.75
<b>FWHM</b>	1.25	2.05	0.85	0.70	1.15	1.00
<b>1.3 ML UHV-grown EG/SiC(0001)</b>						
	<b>Si 1s</b>		<b>C 1s</b>			
<b>Component</b>	<b>Bulk Si</b>	<b>SiO<sub>x</sub></b>	<b>Bulk C</b>	<b>EG</b>	<b>S<sub>1</sub></b>	<b>S<sub>2</sub></b>
<b>Lineshape</b>	$a$ -SGL	SGL	SGL	DS	SGL	SGL
<b><math>\epsilon</math> or <math>a/b</math></b>	0.25,0.09	-	-	0.105	-	-
<b><math>\eta</math></b>	0.55	-	0.20	-	0.10	0.20
<b>E<sub>B</sub> (eV)</b>	1841.65	-	283.80	284.75	285.10	285.75
<b>FWHM (eV)</b>	1.12	-	0.90	0.70	1.1	1.0
<b>1.7 ML Furnace-grown EG/SiC(0001)</b>						
	<b>Si 1s</b>		<b>C 1s</b>			
<b>Component</b>	<b>Bulk Si</b>	<b>SiO<sub>x</sub></b>	<b>Bulk C</b>	<b>EG</b>	<b>S<sub>1</sub></b>	<b>S<sub>2</sub></b>
<b>Lineshape</b>	$a$ -SGL	SGL	SGL	DS	SGL	SGL
<b><math>\epsilon</math> or <math>a/b</math></b>	0.25,0.09	-	-	0.105	-	-
<b><math>\eta</math></b>	0.55	0	0.20	-	0.10	0.20
<b>E<sub>B</sub> (eV)</b>	1841.65	1844.10	283.90	284.80	285.10	285.75
<b>FWHM (eV)</b>	1.1	1.95	0.85	0.64	1.0	0.9

$$DS(x: \varepsilon, f, x_0) = \frac{\cos\left[\frac{\pi\varepsilon}{2} + (1 - \varepsilon)\tan^{-1}\left(\frac{x - x_0}{F}\right)\right]}{[F^2 + (x - x_0)^2]^{(1-\varepsilon)/2}}, \quad \text{Eq. S2}$$

with asymmetry factor  $\varepsilon$ , position  $x_0$ , and width  $F$ .

All spectra were fit using a Shirley background [8]. The asymmetry value  $\varepsilon$  for the EG peak was set to 0.105, consistent with observations from EG from H-intercalated EG/SiC(0001) [9]. Fit parameters for the spectra in Fig. 1 and S8 are provided in Table S1.

### **XSW Analysis Using Conventional C 1s and Si 1s Peak-fitting Models.**

The peak-fitting models used to analyze the data in the main text (and summarized in Table S1) differ substantially from those typically employed [10, 11]. However, we note that the C 1s data from nominally zero-layer graphene presented in Ref. [10] can be well fit by accounting for a small amount of graphene coverage and inverting the  $S_1:S_2$  intensity ratio (Fig. S5). The presence of such graphene inclusions on step edges have been thus far unavoidable during the production of nominally zero-layer graphene, and are observed even on the highest-quality samples grown using state-of-the-art processes in Ar atmosphere [12-14]. We also observe that the data presented in the Ref. [10] was acquired prior to the development of more well-controlled, homogenous EG/SiC(0001) produced by Ar anneal [15], increasing the likelihood of relatively high EG coverage on the samples presented in that work. It is therefore likely that the spectra presented in Ref. [10] should be fit accounting for contributions from EG layers, as is presented in Fig. S5.

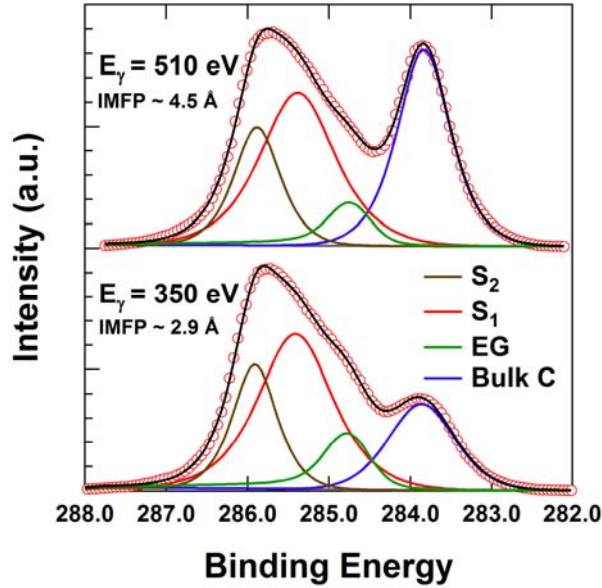


**FIG. S5:** Fits to data from nominal zero-layer graphene on SiC(0001) from Ref. [10], with  $C_{\text{Bulk}}$ , EG,  $S_1$ , and  $S_2$  components in blue, green, red, and brown, respectively. The spectra are fit accounting for a  $\sim 15\%$  coverage of EG. In contrast to Ref. [10], the  $S_1:S_2$  peak intensity ratio is essentially inverted.

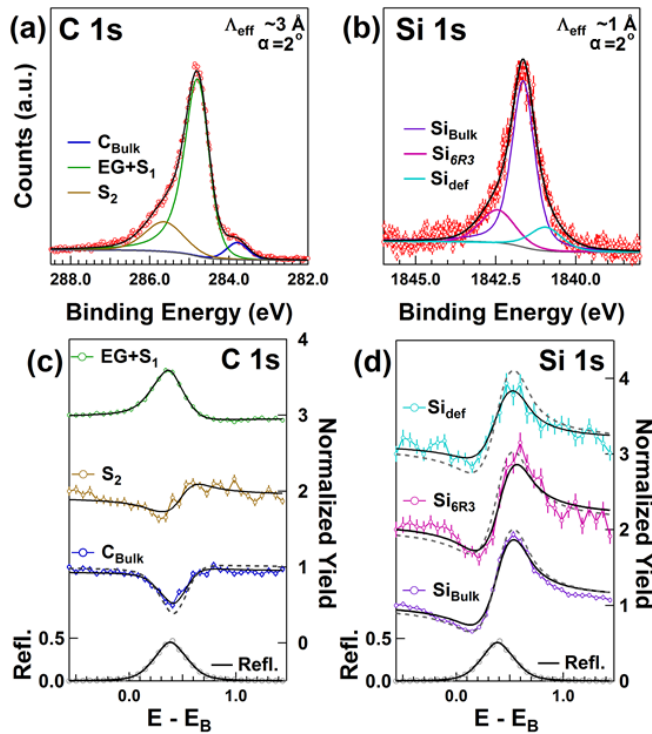


**FIG. S6:** XPS peak-fitting and subsequent XSW data using the fit parameters suggested by Emtsev *et al.* and Riedl. The data presented in these figures are the same as that presented in Figs. 2(c) and (d). (a) The C 1s data were fit with three peaks for XSW analysis because the  $S_1$  and EG peaks were statistically inseparable. (b) The Si 1s peak fitting model shown here accounts for the possible presence of distinct  $6R3$  and defect related core-shifted components. In (c) and (d) the XSW results corresponding to the peak fitting models in (a) and (b), respectively. XPS yield curves are offset on the y-axis for clarity.

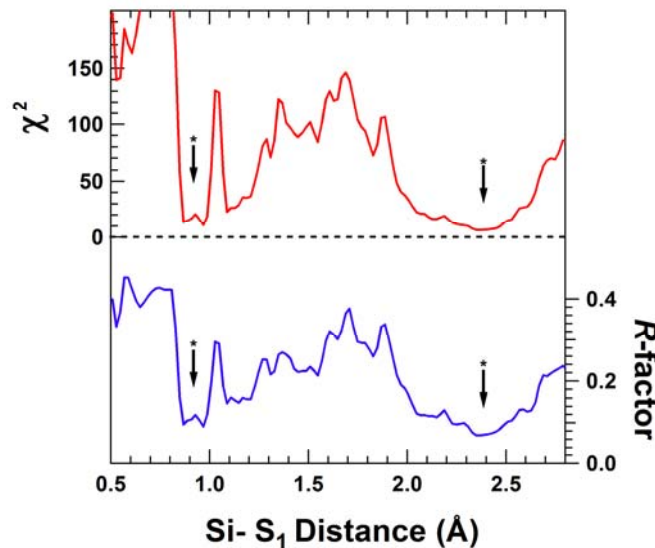


**Figure S7:** Goodness-of-fit maps for the Si-S<sub>1</sub> distance with fixed S<sub>2</sub> position using traditional [10] peak-fitting models. There exist two local minima, indicating possible solutions at Si-S<sub>1</sub> = 0.9 Å, and Si-S<sub>1</sub> = 2.4 Å, but both solutions lack realistic physical interpretation.

Similarly, Riedl *et al.* propose that the Si 2p spectrum be fit with a 3-peak model due to the presence of *6R3* and “defect” species [11]. We note, however, that even a moderate population of surface-specific species would presumably dominate the spectrum in a fashion similar to that observed for the C 1s spectrum, while the observed increase in the relative intensity on the wings of the Si 1s peak are marginal ( $\sim \times 3$ ) when the measurement taken in the  $\alpha \sim 2^\circ$  geometry as compared to that taken in the conventional geometry (Fig. S4). Therefore, we advocate that the increased intensity at the wings does not arise from distinct Si species with discrete, core-shifted components, but is rather caused by the distribution of bond angles and bond lengths present at the strained interface. Finally, we note that in the work of Riedl *et al.*[11], both the *6R3* and “defect” components disappear upon H-decoupling of the buffer layer from the substrate, which is consistent with our interpretation of spectral broadening due to strained Si species.

**Table S2:** XSW results based on XPS peak-fitting models from Refs. [10] and [11]. Reported uncertainties are 1-sigma confidence bounds.

	<b>Component, <math>j</math></b>	$\chi^2$	$P_j$	$z_j(\text{\AA})$	$f_j$	$\sigma_j(\text{\AA})$
<b>C 1s</b>	Bulk C	1.30	$0.76\pm 0.03$	$2.39\pm 0.13$	$0.85\pm 0.1$	$0.23^{+0.07}_{-0.10}$
	EG + $S_1$	1.53	$0.39\pm 0.03$	N/A	$0.22\pm 0.03$	N/A
	$S_2$	2.94	$0.83\pm 0.04$	$2.09\pm 0.10$	$0.65\pm 0.15$	$0.37^{+0.10}_{-0.07}$
<b>Si 1s</b>	Bulk Si	4.85	$1.00\pm 0.02$	$2.52\pm 0.05$	$0.88\pm 0.08$	$0.21^{+0.06}_{-0.1}$
	$Si_{6R3}$	2.15	$0.95\pm 0.06$	$2.42\pm 0.13$	$0.9\pm 0.3$	$0.18^{+0.12}_{-0.08}$
	$Si_{\text{def}}$	0.79	$0.97\pm 0.11$	$2.44\pm 0.25$	$0.6\pm 0.3$	$0.4^{+0.2}_{-0.2}$

Regardless, we are not limited in the analysis of a single peak fitting model, and therefore provide alternate XSW analysis using the XPS models offered by Emtsev and Riedl. The C 1s and Si 1s spectra fit according to these models in shown in Fig. S6. Both spectra are well fit based on the literature values. We note that in Emtsev's model, the  $S_1$  and EG components differ in binding energy by only  $\sim 0.1$  eV. This results in a high degree of covariance of peak fitting parameters for these two species, greatly complicating the XSW analysis. The  $S_2$  component, on the other hand, is practically isolated (core-shifted by +1.1 eV) and can be analyzed in a straightforward manner. The XSW data and fits are presented in Figs. S6(b) and (c), and the results are summarized in Table S2. Because direct analysis of the EG +  $S_1$  component proves impractical (the one measured Fourier component possesses as many as 4 distinct contributions), we explore Emtsev's model by constraining the  $S_2$  species within its XSW-derived 1-sigma confidence window ( $2.0 \text{ \AA} < z_{S_2} < 2.2 \text{ \AA}$ , see Table S2) and mapping the goodness-of-fit  $\chi^2$  and  $R$ -factor as a function of  $z_{S_1}$  between  $0.5 > z_{S_1} > 3.0$ . The resulting  $\chi^2$  and  $R$ -factor maps are shown in Figure S7. There exist two distinct local minima in the map, indicating potential solutions for Emtsev's model at  $z_{S_1} \sim 0.9 \text{ \AA}$  and  $z_{S_1} \sim 2.4 \text{ \AA}$ . The  $z_{S_1} \sim 0.9 \text{ \AA}$  solution would indicate Si-C and graphene-like C-C bonding distances that are incompatible with the interpretation of a partially-

bound graphene-like interfacial layer. The  $z_{S_1} \sim 2.4 \text{ \AA}$  solution produces a structure largely similar to the one presented in the main text, but places the Si-C-C<sub>3</sub> bonded atoms at distances much larger than typical Si-C bond lengths. Furthermore, this model places the Si-C-C<sub>3</sub> bonded C atoms in a highly unphysical bonding geometry, at  $0.3 \text{ \AA}$  *above* the atoms in a graphene-like configuration.

The XSW modulations resulting from the fitting of the Si 1s spectra with distinct, core-shifted, non-bulk-like components are shown in Figure S6(d). The Fourier amplitudes and phases for these three components are practically indistinguishable within error (Table S2), indicating all species have similar positions and distributions with respect to the substrate lattice. While it is possible that this result indicates the existence of small populations (<5% at surface) of distinct chemical species positioned in bulk-like SiC positions, we would expect some non-bulk like XSW modulation of the Si 1s spectral components if any Si-Si bonds were present, and none is observed. An alternate explanation, in which interfacial strain causes increased variance in the distribution of Si-C bond lengths and angles of the topmost Si layers, thereby broadening the Si 1s spectral distribution, is more plausible.

#### **Analysis of 0.5 ML UHV-grown 1.7 ML Ar-grown EG/SiC(0001):**

C 1s and Si 1s spectra taken with emission angle  $\alpha = 2^\circ$  are shown in Fig. S8 for both 0.5 ML UHV-grown [S8(a)-(b)] and 1.7 ML Ar-grown [S8(c)-(d)] EG/SiC(0001). Both samples exhibit C 1s spectra typical of EG/SiC(0001), but both Si 1s spectra also possess a strong high-BE component consistent with SiO<sub>x</sub> chemical species [16]. This signal is only discernible when using the  $\alpha = 2^\circ$  geometry, indicating that it is associated with a surface oxide species. Due to the relatively low spectral resolution of our measurement, we do not attempt to identify sub-oxide

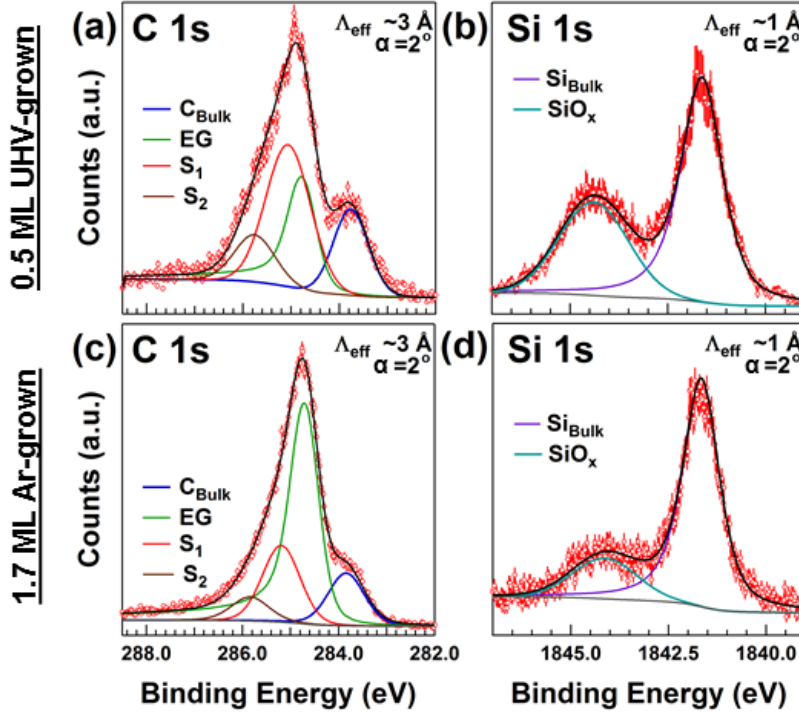


Figure S8: C 1s and Si 1s spectra from 0.5 ML (a)-(b) UHV-grown EG/SiC(0001) and (c)-(d) 1.7 ML Ar-grown EG/SiC(0001).

Table S3: XSW results for 0.5 UHV-grown and 1.7 ML Ar-grown graphene.

UHV-grown 0.5 ML EG/SiC(0001)					
Component, $s$	$\chi^2$	$P_s$	$z_s$ (Å)	$f_s$	$\sigma_s$ (Å)
Bulk Si	2.12	0.99±0.01	2.49±0.03	0.90±0.03	0.18 <sup>+0.03</sup> <sub>-0.03</sub>
SiO <sub>x</sub>	2.03	N/A	N/A	0.1±0.1	N/A
Bulk C	6.22	0.74±0.02	1.87±0.05	0.95±0.08	0.1 <sup>+0.07</sup> <sub>-0.1</sub>
S <sub>1</sub>	1.36	0.9±0.1	2.3±0.2	0.3±0.2	0.6 <sup>+0.2</sup> <sub>-0.2</sub>
S <sub>2</sub>	1.21	0.8±0.05	2.0±0.1	0.9±0.2	0.18 <sup>+0.15</sup> <sub>-0.13</sub>
EG	1.45	0.27±0.04	N/A	0.70±0.3	N/A
Ar-grown 1.7 ML EG/SiC(0001)					
Component, $s$	$\chi^2$	$P_s$	$z_s$ (Å)	$f_s$	$\sigma_s$ (Å)
Bulk Si	0.33	1.00±0.01	2.52±0.03	0.94±0.08	0.1 <sup>+0.07</sup> <sub>-0.1</sub>
SiO <sub>x</sub>	1.09	N/A	N/A	0.0 <sup>+0.2</sup> <sub>-0.0</sub>	N/A
Bulk C	3.37	0.74±0.02	1.87±0.05	0.86±0.07	0.22 <sup>+0.06</sup> <sub>-0.06</sub>
S <sub>1</sub>	3.11	1.00±0.05	2.52±0.13	0.3±0.1	0.6 <sup>+0.1</sup> <sub>-0.05</sub>
S <sub>2</sub>	0.86	0.84±0.03	2.12±0.07	1.00±0.14	0.1 <sup>+0.07</sup> <sub>-0.1</sub>
EG	1.21	0.34±0.04	N/A	0.52±0.09	N/A

signals within the Si 1s, as have been observed previously [16]. We do note, however, that in the case of the 1.7 ML sample, which has a weaker oxide signal, the SiO<sub>x</sub> core-level shift is 0.3 eV less than that of the 0.5 ML sample, suggesting increased contribution from lower-BE sub-oxide species. The oxygen concentration can be estimated by comparing the integrated O 1s signal intensity to that of the EG C 1s signal. The density of C in EG form is estimated from the unit cell definition to be 38.2 C/nm<sup>2</sup>, and therefore, by correcting for the relative C and O photoionization cross-sections at ~2.5 keV, we estimate a concentration of ~2 O/nm<sup>2</sup> for the 1.7 ML Ar-grown sample, and ~6 O/nm<sup>2</sup> for the 0.5 ML UHV-grown sample. For the Ar-grown sample, the oxide formation may be caused by the presence of trace O<sub>2</sub> or H<sub>2</sub>O in the chamber during growth or cool down. In the case of the UHV-grown sample the oxide formation may arise due to exposure of the more reactive sub-ML sample, which has large regions of exposed zero-layer graphene, to air.

XSW results for both samples are shown in Fig. S9, and the results are summarized in Table S3. The most notable result is that for the Si<sub>Bulk</sub>, C<sub>Bulk</sub>, S<sub>1</sub> and S<sub>2</sub> values are essentially identical between all measured samples. Considering that these samples were made using different growth methods, in different laboratories, and possess differing EG and oxide coverage, these nearly identical results are a testament to the ubiquity of the interfacial structure. The SiO<sub>x</sub> components are randomly distributed, indicating that there exists a thick or broadly distributed (as opposed to single oxide monolayer) region of silicon oxide near the SiC surface. The 0.5 ML UHV-grown EG result is interesting as it approaches the value expected for mainly monolayer graphene (at z<sub>EG1</sub> ~5.8 Å, an isolated monolayer would give a coherent position of P<sub>EG1</sub> = 0.30). This, along with the relatively high measured coherent fraction (f<sub>EG</sub> = 0.7±0.3), indicates that most of the EG signal originates from monolayer graphene. Contribution from the second layer

of EG, EG<sub>2</sub> (at  $z_{EG_2} \sim 9.15 \text{ \AA}$ ) would, in principle, shift the Fourier phase positive and reduce the coherent fraction, as is observed for samples with higher EG coverage. It should be noted that the XSW-XPS data for the 0.5 ML sample possess poorer counting statistics, which is reflected in the generally larger degree of scatter in the data and uncertainty values in the extracted XSW results.

The 1.7 ML Ar-grown sample serves to validate the XSW-XRR analysis performed in the main text. Qualitatively, the XSW values for S<sub>1</sub> and S<sub>2</sub> agree extremely well with those in the main text (within 1-sigma in both cases), indicating that the two samples have essentially

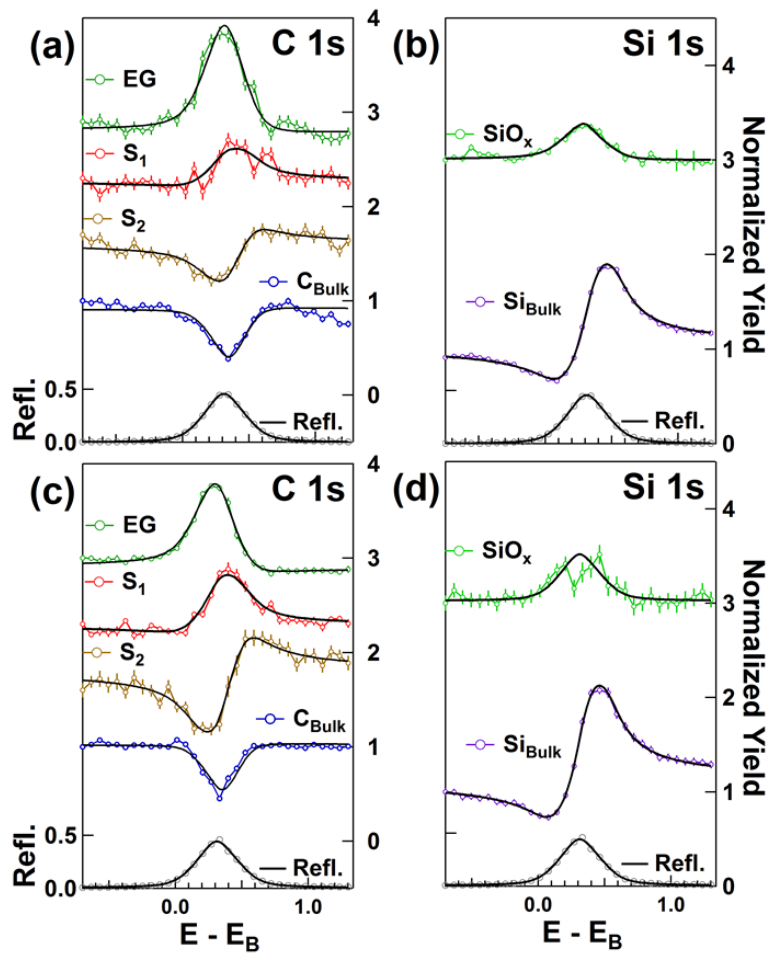


**FIG. S7:** XSW results for (a) C 1s 0.5 ML UHV-grown. (b) Si 1s 0.5 ML UHV-grown. (c) C 1s 1.7 ML furnace-grown. (d) Si 1s 1.7 ML UHV-grown EG/SiC(0001) samples.

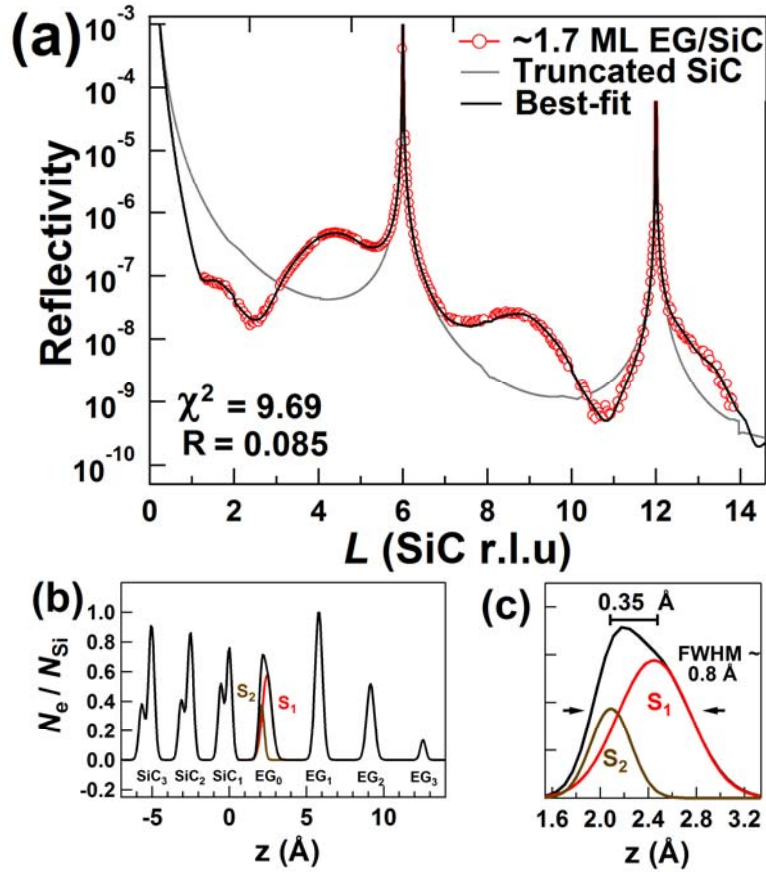


**FIG S8:** XRR analysis for the 1.7ML Furnace-grown EG/SiC(0001) sample. Results are highly comparable to those found in the main text, apart from a higher degree of graphene coverage.

identical interfacial structure. The differing XSW result for the EG component is due to the varying amount of EG coverage on the samples. The XRR data and XSW-constrained best-fit result is shown in Fig. S10. We find that the values  $z_{EG_1} \sim 5.80 \text{ \AA}$ ,  $z_{EG_2} \sim 9.15 \text{ \AA}$ , and  $z_{EG_3} \sim 12.55 \text{ \AA}$  yield  $\chi^2 = 9.69$  and  $R$ -factor = 0.085, comparable to values found for 1.3 ML EG/SiC(0001) of  $\chi^2 = 7.19$  and  $R$ -factor = 0.079 . The slightly poorer quality of the fit for the Ar-grown sample may be attributed to the inability to accurately model the contribution of the  $\text{SiO}_x$  in the electron density profile. Relative layer coverages were  $c_{EG_1} \sim 1.00 \text{ ML}$ ,  $c_{EG_2} \sim 0.55 \text{ ML}$ , and  $c_{EG_3} \sim 0.10 \text{ ML}$ , summing to a total coverage of 1.7 ML. The back-calculation of the XSW values gives  $f_{EG} = 0.38$  and  $P_{EG} = 0.44$ , near the 1-sigma of the uncertainty limits for XSW results reported in Table

S3. In all, the consistency across sample coverage, production method, and sample morphology provides strong support for conclusions stated in the main text.

- [1] J. Zegenhagen, B. Detlefs, T.L. Lee, S. Thiess, H. Isern, L. Petit, L. Andre, J. Roy, Y.Y. Mi, I. Joumard. "X-ray standing waves and hard X-ray photoelectron spectroscopy at the insertion device beamline ID32," *Journal of Electron Spectroscopy and Related Phenomena* **178**, 258-267 (2010).
- [2] J.J. Lee, C.J. Fisher, D.P. Woodruff, M.G. Roper, R.G. Jones, B.C.C. Cowie. "Non-dipole effects in photoelectron-monitored X-ray standing wave experiments: characterisation and calibration," *Surface Science* **494**(3), 166-182 (2001).
- [3] I.A. Vartanyants, J. Zegenhagen. "Quadrupole contribution to the angular resolved photoemission from an X-ray interference field," *Physica Status Solidi B-Basic Research* **215**(1), 819-826 (1999).
- [4] P. Fenter, J.G. Catalano, C. Park, Z. Zhang. "On the use of CCD area detectors for high-resolution specular X-ray reflectivity," *Journal of Synchrotron Radiation* **13**, 293-303 (2006).
- [5] J.D. Emery, Q.H. Wang, M. Zarrouati, P. Fenter, M.C. Hersam, M.J. Bedzyk. "Structural analysis of PTCDA monolayers on epitaxial graphene with ultra-high vacuum scanning tunneling microscopy and high-resolution X-ray reflectivity," *Surface Science* **605**(17-18), 1685-1693 (2011).
- [6] G.K. Wertheim. "Deconvolution and smoothing: Applications in ESCA," *Journal of Electron Spectroscopy and Related Phenomena* **6**(3), 239-251 (1975).
- [7] S. Doniach, M. Sunjic. "Many-electron singularity in X-ray photoemission and X-ray line spectra from metals," *Journal of Physics Part C Solid State Physics* **3**(2), 285 (1970).
- [8] D.A. Shirley. "High-resolution X-ray photoemission spectrum of the valence bands of gold," *Physical Review B* **5**(12), 4709 (1972).
- [9] J.D. Emery, V.D. Wheeler, B. Detlefs, M.E. McBriarty, S.S. Lee, P. Fenter, J. Zegenhagen, D.K. Gaskill, M.J. Bedzyk. "Interfacial Structure of H-intercalated Epitaxial Graphene on SiC(0001)," In Preparation, (2013).
- [10] K.V. Emtsev, F. Speck, T. Seyller, L. Ley, J.D. Riley. "Interaction, growth, and ordering of epitaxial graphene on SiC{0001} surfaces: A comparative photoelectron spectroscopy study," *Physical Review B* **77**(15), 155303 (2008).

- [11] C. Riedl, C. Coletti, T. Iwasaki, A.A. Zakharov, U. Starke. "Quasi-free-standing epitaxial graphene on SiC obtained by hydrogen intercalation," *Physical Review Letters* **103**(24), 246804 (2009).
- [12] C. Riedl, U. Starke, J. Bernhardt, M. Franke, K. Heinz. "Structural properties of the graphene-SiC(0001) interface as a key for the preparation of homogeneous large-terrace graphene surfaces," *Physical Review B* **76**(24), 374009 (2007).
- [13] S. Forti, K.V. Emtsev, C. Coletti, A.A. Zakharov, C. Riedl, U. Starke. "Large-area homogeneous quasifree standing epitaxial graphene on SiC(0001): Electronic and structural characterization," *Physical Review B* **84**(12), 125449 (2011).
- [14] S. Goler, C. Coletti, V. Piazza, P. Pingue, F. Colangelo, V. Pellegrini, K.V. Emtsev, S. Forti, U. Starke, F. Beltram. "Revealing the atomic structure of the buffer layer between SiC (0001) and epitaxial graphene," *Carbon* **51**, 249-254 (2012).
- [15] K.V. Emtsev, A. Bostwick, K. Horn, J. Jobst, G.L. Kellogg, L. Ley, J.L. McChesney, T. Ohta, S.A. Reshanov, J. Rohrl, *et al.* "Towards wafer-size graphene layers by atmospheric pressure graphitization of silicon carbide," *Nature Materials* **8**(3), 203-207 (2009).
- [16] L.I. Johansson, C. Virojanadara, T. Eickhoff, W. Drube. "Properties of the SiO<sub>2</sub>/SiC interface investigated by angle resolved studies of the Si 2p and Si 1s levels and the Si KLL Auger transitions," *Surface Science* **529**(3), 515-526 (2003).